Journal of The Electrochemical Society, **154** (4) A283-A289 (2007)
0013-4651/2007/154(4)/A283/7/$20.00 © The Electrochemical Society

Surface Chemistry of $LiFePO_4$ Studied by Mössbauer and X-Ray Photoelectron Spectroscopy and Its Effect on Electrochemical Properties

Young-Ho Rho,[a] Linda F. Nazar,[b,z] Laura Perry,[b] and Dominic Ryan[b]

[a]*Department of Chemistry, and Department of Physics, University of Waterloo, Waterloo, Ontario, Canada N2L 3G1*
[b]*Department of Physics, McGill University, Montreal, Quebec, Canada H3A 2T8*

$LiFePO_4$ is a promising cathode material for lithium-ion batteries despite its low intrinsic electronic conductivity. We show, using a combination of Mössbauer, X-ray diffraction, and X-ray photoelectron spectroscopy (XPS), that conductive metal phosphides which enhance its electrochemical performance (FeP, and metallic Fe_2P), are generated on the surface of the parent $LiFePO_4$ by reaction with in situ carbon from iron citrate and reducing gases such as hydrogen. Their relative fraction, nature, and location was quantified. Under the most mild reducing conditions, nanosized FeP is formed on the surface along with Li_3PO_4, and carbon resulting from the precursor. Under more aggressive reducing conditions, FeP is still present, but thermodynamics now favor the formation of Fe_2P, with fractions varying from 4 to 18 wt % depending on the temperature and atmosphere used for treatment. Both large (0.5 μm) crystallites, and amorphous or nanodimensioned particles are present. XPS studies reveal that the amorphous or nanodimensioned Fe_2P lies on the inner surface adjacent to the $LiFePO_4$, and the residual carbon lies on the outer surface. The resulting $LiFePO_4$ "composites" show significantly enhanced electrochemical rate properties as well as outstanding cyclability, which allows a high discharge capacity of ~105 mAh g^{-1} at a 14.8C rate (2500 mA g^{-1}).
 [DOI: 10.1149/1.2433539]

Manuscript submitted June 8, 2006; revised manuscript received November 6, 2006. Available electronically February 9, 2007.

$LiFePO_4$, proposed by Padhi et al. in 1997, has come into the spotlight as an alternative to $LiCoO_2$ due to its low cost, nontoxic properties, and safety advantages.[1] Unfortunately, the low intrinsic electronic conductivity of $LiFePO_4$ has been an obstacle to its unequivocal success. Because of the power limitations this presents, much interest has been focused on improving its rate capability for practical applications. Many effective approaches have been introduced, including minimizing the particle size using various synthesis techniques, and forming conductive carbon coatings on the particles by firing them with organic additives.[2-4] A doping technique was also proposed as a method to improve the electrochemical performance, where a dramatic increase of the intrinsic electronic conductivity was proposed to occur by the formation of hole carriers in the lattice. We have demonstrated that promotion of the electronic conduction by formation of metallic compounds such as Fe_2P on the phosphate surface occurs during the doping process, via reduction in the subsequent heat treatment step. This leads to an increase in conductivity of seven orders of magnitude in the bulk composite phase.[5] Thus, in the doped olivine compositions, the enhanced electronic transport is caused primarily by this nanophase phosphide network via conduction at the grain boundaries, rather than a mixed-valent metal $M^{3+/2+}$ state in the bulk. Insulating $LiNiPO_4$ was similarly shown to form surface metallic Ni_3P by reduction, with a concomitant fivefold increase in conductivity.[5] A recent report on lithium nickel phosphate which determined the Ni^{3+}/Ni^{2+} redox potential to be between 5.1 and 5.3 V by cyclic voltammetry,[6] in agreement with theoretical predictions, confirms the importance of such conductive metal phosphides to access electrochemical activity.[5]

In addition to the electronic conductivity of $LiFePO_4$, ionic conductivity is important. At present, this has not been unequivocally determined due to the difficulty in measuring a lithium diffusion coefficient within a two-phase system. The one-dimensional lithium-ion diffusion is thought to be high based on calculations of unconstrained ion transport,[7] but the material appears to behave as a slow ion conductor.[8] Nonetheless, $LiFePO_4$ in the form of sub-μm or nanoparticles to minimize the path length for transport is still very attractive if its electrochemical properties are enhanced. This is irrespective of the lithium ionic conductivity whose improvement is more difficult than that of the electronic conductivity.

In this work, $LiFePO_4$ prepared by a citric sol-gel method[9] was treated in inert and reducing atmospheres (7% H_2 in N_2) in order to investigate the effect of Fe_2P on rate capability and specific capacity. Fe_2P is a metal,[10] which can play a major role in an improvement of the bulk conductivity of $LiFePO_4$, compared to that of the semiconducting amorphous carbon formed at the intermediate processing conditions, which typically displays conductivity on the order of $<10^{-3}$ S cm^{-1}. The amounts of Fe_2P (and FeP) were quantified by Rietveld analysis and Mössbauer spectroscopy, and the nature of the surface was probed by X-ray photoelectron (XPS) spectroscopy. Our report describes the effect of the metallic surface phosphide of $LiFePO_4$ on electrochemical performance.

Experimental

Synthesis.— $LiFePO_4$ was prepared by a sol-gel method using lithium phosphate (Li_3PO_4, Aldrich Chemical Company, Inc.), phosphoric acid ($0.85H_3PO_4 \cdot 0.15H_2O$, Fisher Scientific), and ferric citrate, *n*-hydrate ($FeC_6H_8O_7 \cdot nH_2O$, J.T. Baker Chemical Co.) as starting materials. Lithium phosphate (0.03 M) and phosphoric acid (0.06 M) were mixed together and dissolved in 300 mL of water with the help of sonication. Ferric citrate *n*-hydrate (0.09 M) was dissolved in 500 mL of boiling water, and the two solutions were combined and concentrated on a hot plate until a wet gel with high viscosity was formed. The wet gel was placed in an oven and heated at 140°C for 12 h. The dried gel was ground before firing at a heating rate of 10°C min^{-1}, and the samples were air quenched to obtain crystallized $LiFePO_4$. Samples were prepared under the following different firing conditions: (*i*) 600°C for 1 h in Ar, (*ii*) 600°C for 15 h in Ar, (*iii*) 600°C for 24 h in 7% H_2 in N_2 after firing at 600°C for 15 h in Ar, and (*iv*) at 800°C for 1 h in 7% H_2 in N_2 after firing at 600°C for 15 h in Ar. A residual carbon content of ~8 wt % was determined in all the samples after firing by chemical analysis, independent of the treatment conditions (Table I). This was approximately constant for all materials.

Table I. List of residual carbon content for samples A → D determined by chemical analysis.

	Sample A	Sample B	Sample C	Sample D
Carbon content (wt %)	7.88	8.76	8.38	8.13

[z] E-mail: lfnazar@uwaterloo.ca

Physical characterization.— X-ray diffraction (XRD) measurements were carried out on a Siemens D500 X-ray diffractometer using Cu Kα radiation (wavelength, λ = 1.5405 Å). GSAS software was used for Rietveld refinements of the diffraction patterns to determine the ratio of $LiFePO_4$, FeP, Fe_2P, and Li_3PO_4.[11] Scanning electron microscope (SEM) images were obtained on an LEO 1530 FE-SEM with energy dispersive analysis (EDAX) to observe surface morphologies and composition. The room-temperature Mössbauer spectra were recorded in transmission mode using a 50 mCi $^{57}Co/Rh$ source, on powders contained in a holder with the sample loading adjusted to be ~10 mg cm^{-2}. Velocity and isomer shift calibrations were performed using Fe foil as a standard. Spectra were fitted to a sum of Lorentzian lines using a conventional nonlinear least-squares minimization routine. Each component was fitted with an independent linewidth to accommodate possible differences in disorder within each phase.

XPS analysis was performed using a multitechnique ultrahigh vacuum Imaging XPS Microprobe system (Thermo VG Scientific ESCALab 250) equipped with a hemispherical analyzer (of 150 mm mean radius) and a monochromatic Al Kα (1486.6 eV) X-ray source. The high sensitivity of this instrument obtained at a routine instrumental energy resolution of 0.5 eV full width at half maximum (FWHM) at 20 eV pass energy allows us to easily characterize spectral features in the core-shell regions. The spot size for the XPS analysis used for the present work was approximately 0.5 × 1.0 mm. Photoelectrons were detected in the normal emission direction with an effective acceptance angle of ca. ± 25° from the surface normal. After pelletizing the powder at high pressure, the samples were mounted on a stainless-steel sample holder with double-sided carbon tape. The chamber was maintained at a pressure of less than 10^{-10} mbar. Curve fitting was performed using CasaXPS VAMAS processing software and the binding energies of individual elements were identified with reference to the NIST X-ray Photoelectron Spectroscopy Database (NIST Standard Reference Database 20, version 3.4, web version).[11] Ar^+ ion beam sputtering for surface etching was carried out in order to observe the surface state of samples.

Electrochemistry.— The electrochemical performance of the cathodes was evaluated using a coin-type cell (size 2220) with a lithium metal anode. The cathode consisted of the active material, carbon black (Conductex SC carbon), and polyvinylidene fluoride (PVdF) with weight ratio of 85:10:5. The electrolyte was a mixed solvent of ethylene carbonate and dimethyl carbonate (1:1) containing 1 mol dm^{-3} $LiPF_6$. The typical loading of $LiFePO_4$ was ~5 mg in each cell. Carbon-coated aluminum foil used as a current collector was supplied from IntelliCoat, USA. The galvanostatic charge and discharge experiments were conducted with a MacPile (Biologic S.A., Claix, France), with cutoff voltages set to be 4.5 and 2.2 V for charge and discharge, respectively. The theoretical capacity of the active material was determined based on the Fe^{2+}/Fe^{3+} redox reaction in $LiFePO_4$, which corresponds to 170 mAh g^{-1}. Constant charge and discharge current rates are used with the *C*-rate convention, or *C*/*n*, where *n* is the time in hours for complete charge-discharge, that is, 1 C rate is equivalent to 170 mA g^{-1}. No trickle charging was applied in this work.

Results and Discussion

Citric acid is known as a foaming agent and has been used in order to obtain many porous materials.[12] Through the citric sol-gel method used here for the synthesis of $LiFePO_4$, spongelike particles were formed in the drying process which then crystallized during firing. The pore size and particle morphology strongly depend on the drying conditions, e.g., time and temperature. In addition, citric acid also acts as an agent to reduce the Fe^{3+} to Fe^{2+}, and successfully prevents Fe^{2+} from oxidation.

The diffraction patterns of the resultant materials shown in Fig. 1 indicate that all of the samples can be characterized as $LiFePO_4$ with an olivine structure, and that additional heat treatment under 7% H_2 in N_2 promotes the generation of Fe_2P/FeP and Li_3PO_4 by the reduction of $LiFePO_4$. The Fe_2P is visible in the diffraction pattern of samples C and D (strongest lines indicated by the arrows), whereas the FeP is barely visible in the pattern of sample C, although olivine reflections obscure some of the contributions. FeP and Fe_2P are thermodynamically stable at 600 and 800°C, respectively; FeP is transformed into Fe_2P above 600°C by the vaporization of phosphorus.[13] The formation of the metallic Fe_2P on the surface of $LiFePO_4$ therefore takes place by one of the following reduction reactions, depending on the temperature

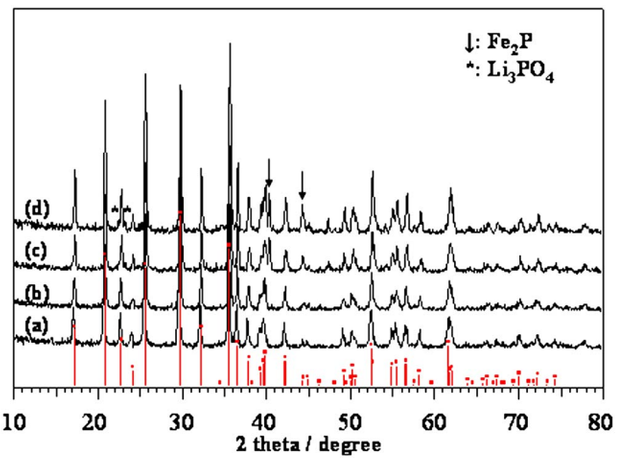

Figure 1. (Color online) XRD patterns of the $LiFePO_4$ samples fired at (a) A: 600°C for 1 h in Ar, (b) B: 600°C/15 h/Ar, (c) C: 600°C/15 h/Ar, followed by 600°C/24 h/7% H_2/N_2; (d) D: 600°C/15 h/Ar, followed by 800°C/1 h/7% H_2/N_2. The arrows indicate the position of the strongest lines of Fe_2P. FeP is barely detectable in the pattern of sample C (see Fig. 2 for details of FeP contributions).

Carbothermal

$$6LiFePO_4 + 8C(16C) \rightarrow 2Fe_2P + 2Li_3PO_4 + 2FeP + 8CO_2\uparrow \text{ (or } 16CO\uparrow) \quad [1a]$$

$$\rightarrow 3Fe_2P + 2Li_3PO_4 + P\uparrow \quad [1b]$$

where the citric acid residue participates as the carbon source,[5,14] or Hydrogen reduction

$$6LiFePO_4 + 16H_2 \rightarrow 2Fe_2P + 2Li_3PO_4 + 2FeP + 16H_2O\uparrow \quad [2a]$$

$$\rightarrow 3Fe_2P + 2Li_3PO_4 + P\uparrow \quad [2b]$$

The carbothermal (or hydrogen) reduction carried out under fewer forcing conditions (lower temperature) is described by Eq. 1a, where both Fe_2P and FeP are formed, giving rise to a 2:2 molar ratio of Fe_2P to Li_3PO_4. Under more forcing conditions, described by Eq. 1b, elemental phosphorus is released, and complete conversion of FeP to Fe_2P occurs, i.e., "full" reduction, which gives rise to a 3:2 molar ratio. At lower temperatures, Reaction 1a predominates, whereas at higher temperatures, Reaction 1b predominates: Both Reactions 1 and 2 are operative in this study. The process implies sequential formation of $LiFePO_4$ followed by reduction to form phosphides, but the formation of iron phosphide may accompany the formation of olivine at high processing temperatures under reducing conditions.

Because it is important to find the exact mass of the active material in order to precisely evaluate the inherent electrochemical capacity, Rietveld refinement of the XRD data was carried out to quantify the fraction of $LiFePO_4$ and the crystalline products (Fe_2P, FeP,

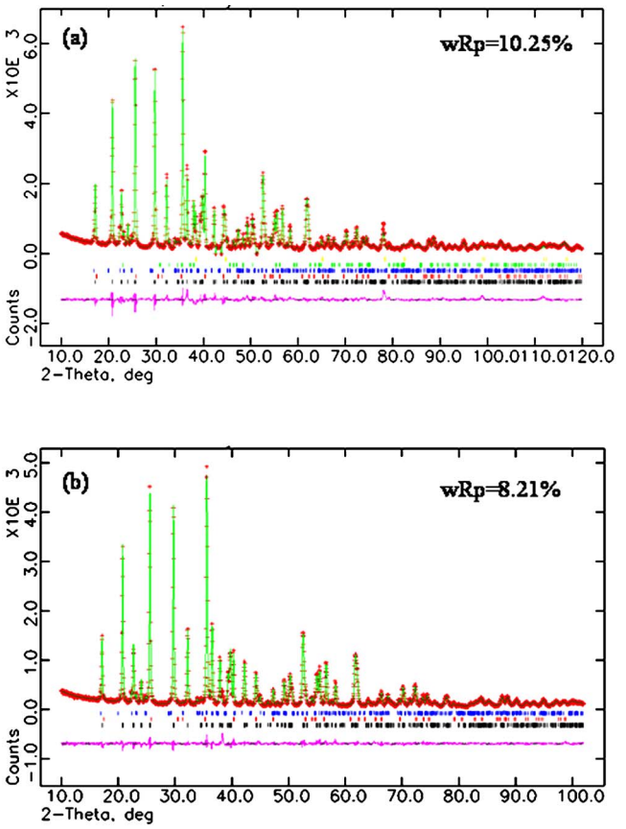

Figure 2. (Color online) Rietveld analysis of XRD patterns of (a) sample C fired at 600°C/15 h/Ar followed by 600°C/24 h/7% H_2/N_2, (b) sample D fired at 600°C/15 h/Ar, followed by 800°C/1 h/7% H_2/N_2. The patterns were refined as a mixture of: $LiFePO_4$ (black tick marks, refined cell: a = 10.3275 Å; b = 6.0075 Å; c = 4.6961 Å), Li_3PO_4 (blue tick marks, refined cell: a = 6.0801 Å; b = 10.5381 Å; c = 4.9533 Å), and Fe_2P (red tick marks, refined cell: a = 5.8741 Å; b = 5.8741 Å; c = 3.4522 Å; α = 90°; β = 90°; γ = 120°). In sample C, FeP (green tick marks, refined cell: a = 5.1930 Å; b = 5.7920 Å; c = 3.0990 Å) is also apparent. The phase fractions from the refinements are listed in Table II.

and Li_3PO_4). Rietveld analyses for samples A and B showed that the phosphide level was too low to readily discern, and only $LiFePO_4$ was apparent in the pattern. Samples C and D showed detectable levels of crystalline phosphide, however. The fits and resulting phase fractions shown in Fig. 2 are summarized in Table II. As explained above, based on the theoretical calculation from the expected decomposition reaction, the molar ratio between Fe_2P and Li_3PO_4 should be ~3:2 (equivalent to a ~2:1 weight ratio) at "full" reduction (Eq. 1a) or a 2:2 molar ratio (equivalent to a 1.5:1 weight ratio) for an incomplete reaction (Eq. 1b). However, the weight ratio determined from Rietveld was much less, namely close to 1:1 (or below) for both samples (Table II). This means that amorphous or nanosized compounds (mainly iron phosphide) are included in the products which are undetectable by XRD.

Table II. The weight percentage of $LiFePO_4$ and impurity phases obtained from a multiphase Rietveld refinement of the XRD data for samples C and D.

Unit: wt %	$LiFePO_4$	FeP	Fe_2P	Li_3PO_4
Sample C	81.4	1.5	9.1	8.0
Sample D	87.8	-	5.0	7.2

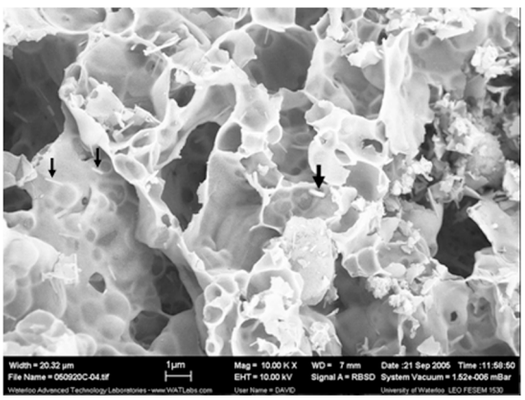

Figure 3. SEM image of $LiFePO_4$, sample C. The arrows (↓) indicate Fe_2P crystallites.

The SEM image in Fig. 3 shows the typical porous morphology of $LiFePO_4$ prepared by the citric sol-gel method. This was observed for fall of the samples independent of the firing conditions, meaning that the citric acid successfully acts as foaming agent, and that drying to form the gel powder is critical for pore formation as mentioned above. The thin-walled honeycomb motif is expected to show advanced electrochemical performance: details will be discussed later in the Electrochemical section. A few well-defined platelike crystallites are visible embedded in the thin $LiFePO_4$ honeycomb wall structure in samples C and D, indicated by an arrow (↓) in the image for D (Fig. 3). Spot EDX analysis showed the central hexagonal-shaped particle was iron-rich, indicating it contributes to the crystalline Fe_2P phase seen in the diffraction pattern. This shows that bulk Fe_2P can segregate from the $LiFePO_4$ under the most rigorous heat treatment conditions, as previously reported.[15] This is not inconsistent with our finding that amorphous iron phosphides also coat (or wet) $LiFePO_4$ particles formed using solid-state synthesis methods.[5] Although lithium phosphate must also be present, because reduction yields both Li_3PO_4 and Fe_2P, EDX failed to detect any evidence of phosphorus-rich/iron-poor regions corresponding to Li_3PO_4 on the surface of the sol-gel honeycomb structure. Nonetheless, both of these phases were detected in the XRD, implying that amorphous or nanoscaled phosphide exists together with some glassy or poorly crystallized Li_3PO_4. That is, some large Fe_2P crystallites are segregated from the $LiFePO_4$ but others are finely distributed on the surface as amorphous or nanoscaled particles intimately mixed with Li_3PO_4. The former can be, of course, easily detected by XRD and the latter would be undetectable except by TEM. This necessitates the use of another physical method that is relatively independent of crystallinity so that the entire sample is probed.

Mössbauer phase analysis.— Mössbauer is particularly sensitive to a morphous phases and nanoscale phases. Figure 4 shows the Mössbauer spectra obtained for sample A, B, C, and D prepared by heat treatment under progressively more reducing conditions (A → D). The resulting Mössbauer parameters are shown in Table III, and the fraction of the components is listed in Table IV. For all samples, one symmetric doublet was dominant with an isomer shift (IS) = 1.23 mm/s, which is typical for octahedral Fe^{2+} in ionic compounds ($LiFePO_4$).[16] The large quadrupole splitting (QS) = 2.99 mm/s is due to the high spin configuration of 3d electrons and the asymmetric local environment at the Fe atoms. Another minor doublet corresponding to FeP is resolved in all samples, whose parameters are very close to the literature values of 0.50 mm/s, with a QS of 0.7 mm/s.[17] Note there is uncertainty in the exact fitted values of this phase (and its relative area) due to its very small fraction. For samples D, C, and B (but not A) the Möss-

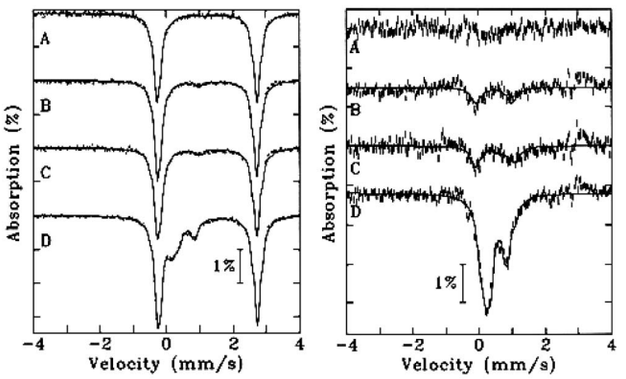

Figure 4. Mössbauer spectra for samples fired at: (A) 600°C/1 h/Ar, (B) 600°C/15 h/Ar, (C) 600°C/15 h/Ar, followed by 600°C/24 h/7% H_2/N_2, (D) 600°C/15 h/Ar followed by 800°C/1 h/7% H_2/N_2. The entire spectrum is shown on the left, and the spectra after subtraction of the $LiFePO_4$ component are shown on the right.

bauer spectrum also reveals the presence of Fe_2P. The structure has two distinct Fe sites, which were fitted in sample D with IS_1 = 0.620 mm/s, QS_1 = 0.427 mm/s, IS_2 = 0.17 mm/s, and QS_2 = 0.12 mm/s, consistent with previously reported values (IS_1 = 0.6 mm/s, QS_1 = 0.427 mm/s, IS_2 = 0.182 mm/s, and QS_2 = 0.088 mm/s).[17] Thus, the material treated under the most mild conditions (sample A: 600°C for 1 h in Ar) shows the presence of a small fraction of FeP, but not Fe_2P, whereas the materials that experienced more rigorous reducing conditions all show the presence of both FeP and Fe_2P. However, the IS and QS for Fe_2P in sample B have relatively large uncertainties because it again contributes only a very small percentage of the overall spectrum and is not well resolved. For the materials treated under the most reducing conditions (sample C: 15 h @600°C in Ar and 24 h @600°C in 7% H_2/N_2; sample D:15 h @600°C in Ar and 1 h 800°C in 7% H_2/N_2), there is a large fraction of Fe_2P along with FeP. Hence, the uncertainties are smaller and the Mössbauer parameters are very close to values reported for the bulk phases.

The ratio between the iron-containing components can be calculated from the areas of each spectral component (Table IV), but to determine the exact ratio between all of the components, the iron-free product of the reduction (Li_3PO_4) also needs to be taken into account. For every mole of $LiFePO_4$ that is reduced, 1/3 of a mole of Li_3PO_4 is produced because the formation of iron phosphide follows the stoichiometry of Reactions 1 and 2. The amount of lithium phosphate is equal to 1 × (*x* mol % of FeP) + 2 × (*y* mol % of Fe_2P). For example, sample D contains 2.4 mol % of FeP and 16.9 mol % of Fe_2P from the Mössbauer measurement (Table IV). Therefore 12.1 mol % Li_3PO_4 (36.4 atom % Li) is simultaneously formed.

Table III. Summary of Mössbauer experimental results for samples A → D; isomer shifts (upper) and quadrupole splitting (lower).

	Fe_2P (I)	Fe_2P (II)	FeP	Fe^{2+} ($LiFePO_4$)
Sample A	-	-	0.45(2)	1.232(1)
Sample B	0.74(7)	−0.01(1)	0.49(2)	1.230(1)
Sample C	0.576(7)	0.1(1)	0.6(3)	1.242(1)
Sample D	0.620(5)	0.17(4)	0.7(1)	1.230(1)
Isomer shift unit: mm/s				
Sample A	-	-	1.08(3)	2.979(2)
Sample B	0.27(9)	0	1.27(6)	2.983(2)
Sample C	0.44(1)	0.2(3)	0.8(6)	2.987(2)
Sample D	0.427(9)	0.12(8)	0.9(2)	2.998(1)
Quadrupole splitting unit: mm/s				

Table IV. The percentage of $LiFePO_4$ and other impurities obtained from the Mössbauer experiments, expressed as mol % (upper) and wt % (lower). The errors in the measurement arising from the fitting procedure are ∼2% of the value given.

Unit: mol %

	$LiFePO_4$	FeP	Fe_2P	Li*X*[a]
Sample A 600°C for 1 h in Ar	94.9	5.1	0.0	5.1
Sample B 600°C for 15 h in Ar	91.2	4.8	4.0	12.8
Sample C 600°C for 15 h in Ar +600°C for 24 h in 7% H_2/N_2	74.6	4.5	20.9	46.3
Sample D 600°C for 15 hin Ar +800°C for 1 h in 7% H_2/N_2	80.7	2.4	16.9	36.2

Unit: wt %

	$LiFePO_4$	FeP	Fe_2P	Li_3PO_4[b]
Sample A 600°C for 1 h in Ar	95.9	2.8	0.0	1.3
Sample B 600°C for 15 h in Ar	90.7	2.6	3.6	3.1
Sample C 600°C for 15 h in Ar +600°C for 24 h in 7%H_2/N_2	69.5	2.3	17.6	10.6
Sample D 600°C for 15 h in Ar +800°C for 1 h in 7% H_2/N_2	76.0	1.2	14.4	8.4

[a] = 1 × (*x* mol % of FeP) + 2 × (*y* mol % of Fe_2P).
[b] Calculated from (*z* mol % of Li*X*)/3.

The final ratio between $LiFePO_4$ and the reaction products is 76:14(FeP:Fe_2P:Li_3PO_4 = 1.2:14.4:8.4) by weight. This analysis is necessary to evaluate the electrochemical performance of the active material, $LiFePO_4$, based on its composition.

We note that the ratio between $LiFePO_4$ and the other phases in Table IV is lower than that in Table II because a greater iron phosphide contribution was determined by the Mässbauer measurements than by the Rietveld refinement of the XRD data. This confirms the presence of either amorphous or nanocrystalline iron phosphide. We expect the latter, because amorphous $Fe_{67}P_{33}$ is reported to have a very different Mössbauer spectrum from that of crystalline Fe_2P, showing a much broader ill-defined line shape.[17] We did not see evidence of this.

XPS studies of the crystallite surface.— The aim of the XPS investigation was to investigate the location of the phosphide and carbon components in sample D, by comparing the as-received material with material whose surface is stripped away by surface etching. The results are shown in Fig. 5. The C 1s spectrum before etching (Fig. 5i) shows the presence of graphitic-like carbon on the surface (peak at 284.5 eV) resulting from the residue from the citric acid.[18] The O 1s spectra and P 2p spectra exhibit features at 531.6 and 133.5 eV [Fig. 5b and 5c(i), respectively] due to the phosphate moitie. The *P* 2p peak contains overlapped contributions from Li_3PO_4 (133.6 eV) (Ref. 19) arising via surface reaction, and $LiFePO_4$ (133.2 eV).[18] The Fe 2p spectrum [Fig. 5d(i)] shows only the expected lines from triphyllite at 711.0 and 724.1 eV (Fe $2p_{3/2}$, $2p_{1/2}$ lines). We expect the Li 1s peak to be slightly higher in energy than in Li_2O (54 eV),[20] according to empirically derived predictions of the direction of the binding energy shift for a cation based on changes in the covalency-ionicity.[21-23] However, the peak is buried under the Fe 3p component that lies in the same region at 55.5 eV,[19,24] and which has ∼13 times greater relative atomic sensitivity.[25] Indeed, we find the Li 1s peak at 56.4 eV in $LiMnPO_4$ where such an overlap does not occur (spectrum not shown).

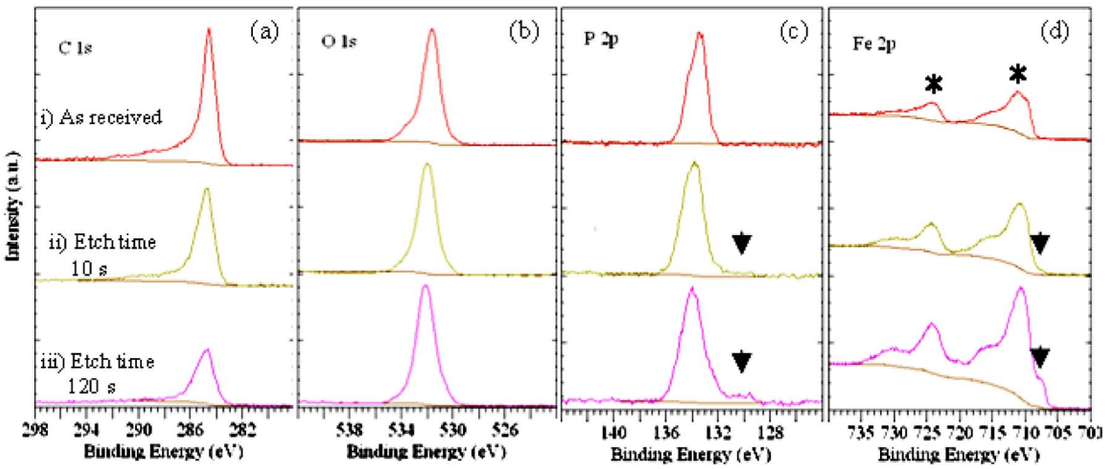

Figure 5. (Color online) XPS spectra of sample D, where in each panel, samples are: (i) as-prepared, (ii) Ar^+ sputtered for 10 s, and (iii) Ar^+ sputtered for 120 s: (a) C 1s spectra: note that very weak peaks at ~290 and ~285 eV are attributed to carbonates and hydrocarbon contaminants, respectively (Refs. 29 and 30); (b) O 1s spectra: note the weak peak at 533.2 eV is due to adsorbed water on the surface, (c) P 2p spectra, (d) Fe 2p spectra. Arrows (↓) in the P 2p and Fe 2p spectra indicate the binding energies for Fe_2P, and the asterisk (*) indicates the binding energies for the Fe $2p_{3/2}$ and Fe $2p_{1/2}$ lines.

The spectra shown in the bottom two panels of Fig. 5: (ii) and (iii) depict the XPS spectra after Ar^+ sputtering, using etch times of 10 and 120 s. The intensity of the C 1s peak at 284.5 corresponding to graphitic carbon decreases with etching, indicating that the carbon mainly exists on the outer surface as expected. Virtually no change occurred in the O 1s spectra except for the decrease of the peak at 533.2 eV corresponding to adsorbed water. However, notable changes were observed in the P 2p and Fe 2p spectra, where no phosphide contribution was visible in the unetched sample. After etching, peaks [↓ in Fig. 5(ii, iii)] appear at 129.5 eV in the P 2p spectra (Fig. 5c, arrows) and at 707.1 eV in the Fe 2p spectra (Fig. 5d, arrows), which increase upon prolonged etching. These features correspond to Fe_2P, in exact agreement with the literature values.[19,26] The increase in intensity of the lines due to Fe_2P (arrow) and $LiFePO_4$ (*) in Fig. 5d shows that both components are uncovered during the sputtering process, suggesting that they lie below the outer surface. The P 2p signal does not change significantly, however. This is due to both Li_3PO_4 components (which are removed by sputtering) and $LiFePO_4$ (which is uncovered by sputtering).

We note that the phosphide contribution in the P 2p spectra (Fig. 5c) is poorly resolved except at long sputtering times, and is "smeared out" in the region between 130–132 eV that lies above the peak. We ascribe this to some small degree of oxidation of the Fe_2P that would slightly increase the binding energy.[19,27] This might occur upon Ar^+ sputtering because it can release oxygen from the surrounding phosphate matrix; such reactivity has been reported in the case of indium phosphites.[27]

Because the XPS peak area corresponds to the relative fraction of the components, these can be quantitatively analyzed as taking the relative atomic sensitivity into account.[25] The atomic ratio of the components with etching time is calculated and summarized in Table V. However, the lithium content could not be obtained due to the aforementioned overlap. The ramifications of the surface components are discussed below with respect to electrochemical performance.

Electrochemistry.— Phosphide content.— Figure 6a shows the comparative electrochemical cycling performance of all samples at 1 C. The cells were all prepared at loadings of approximately 5 mg/cm^2, using electrode material with a density of about 1.0 g/cc formed by compression of the active material prior to electrode construction. The content of the active $LiFePO_4$ required to calculate the specific electrochemical capacity of the samples was taken from Table IV, and the charge-discharge current rate of 1 C was calculated based on the theoretical capacity of $LiFePO_4$ of 170 mAh g^{-1}. The discharge capacity strongly depends on the Fe_2P content. The discharge capacity at 1 C is ~90 mAh g^{-1} for sample A (containing no Fe_2P), 110 mAh g^{-1} for sample B (~3.6% Fe_2P), and ~130 mAh g^{-1} for samples C and D (14 and 18 wt % Fe_2P, respectively). Other factors can be discounted, because the carbon and FeP content of all the samples were very similar (except sample D which contained about half the FeP) and their morphologies were the same. In comparing samples A and B, we see that a small amount of Fe_2P (3.6%) increases the capacity by almost 25%; however, increasing that phosphide percentage by a factor of 4 (sample A → sample C) only increases the capacity by 45%. The effect is, not surprisingly, nonlinear as illustrated in Fig. 6b. The capacity increase is "saturated" after about 14 wt % Fe_2P is reached, which is probably above the percolation threshold necessary for electronic conduction,. Therefore, the optimal Fe_2P content appears to lie between 5–10 wt % for practical applications, and probably closer to the lower value.

Rate capability.— Further electrochemical investigation was carried out on sample D to determine the rate capability of the material with a large fraction of conductive phosphide. The red data points in Fig. 7a show the electrochemical properties at various charge-discharge current rates ranging from 0.11 C (18.7 mA g^{-1}) to 14.8 C (2516 mA g^{-1}). The electrochemical capacity at the highest current rate of 14.8 C (2516 mA g^{-1}, complete charge or discharge in ~4 min) is over 100 mAh g^{-1} (ca. 105 mAh g^{-1}) even after the 150th cycle. This value is ~62% of theoretical capacity, with an energy density estimated to be ~368 Whk g^{-1} and a power density of ~5440 Wk g^{-1}. These are high values, although they were achieved for thin film (low loading) cell configurations. Figure 7b

Table V. Atomic concentration (%) of the elements except lithium for $LiFePO_4$ with metallic conductive surface. The contents were calculated from the intensity of the Fe 2p, P 2p, O 1s, and C 1s peaks with consideration of their relative atomic sensitivity factor (Ref. 19).

Sputtering time (s)	Fe	P	O	C
0	6.2	8.0	31.4	54.4
10	11.2	12.5	34.1	42.2
120	18.0	14.3	38.5	29.2

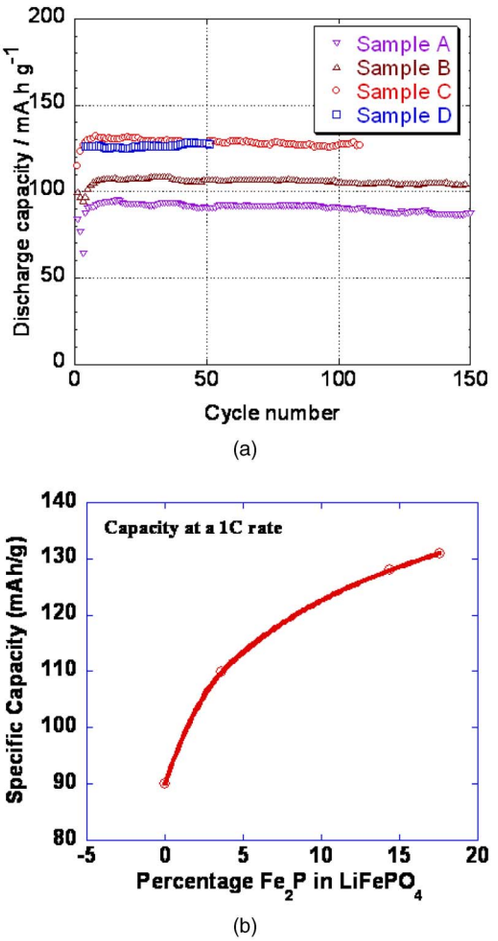

Figure 6. (Color online) (a) Electrochemical cycling performance for samples A → D at a 1 C rate; (b) plot of specific capacity at a C rate vs percentage of Fe_2P in $LiFePO_4$.

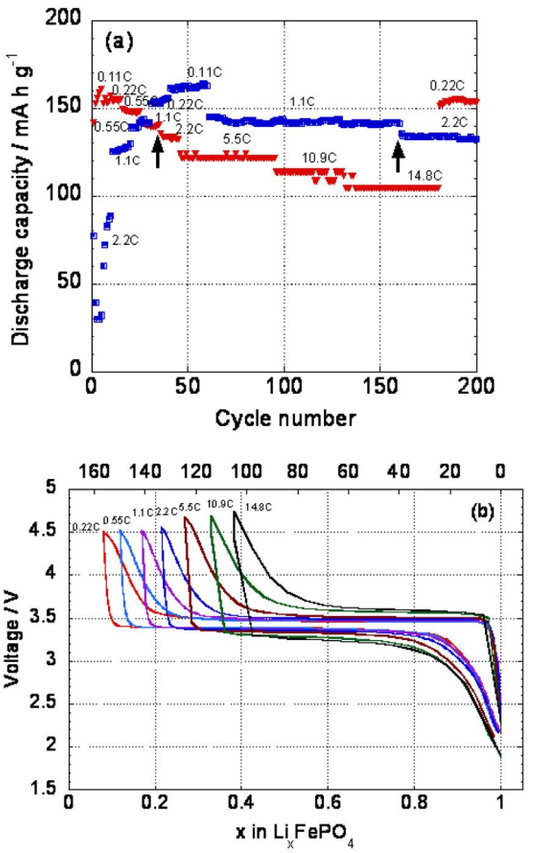

Figure 7. (Color online) (a) Electrochemical cycle performance and (b) charge-discharge curves at different current rates for sample D.

shows the charge and discharge curves corresponding to the different current rates. Well-defined, flat voltage plateaus were obtained for all current density experiments, although the polarization increased from 0.08 to 0.36 V as the current rate increased from 0.22 to 14.8 C.

Electrode conditioning.— Although very good electrochemical performance was obtained for many materials in this study, the charge-discharge curves during the first few cycles were often associated with a large polarization and poor irreversibility which improved markedly upon cycling. For example, it is evident from Fig. 7a that the capacity undergoes an initial increase before stabilizing at a higher value. Thus, starting at low current rates (red data points), the first discharge capacity at 0.11 C (18.7 mA g^{-1}) of 142 mAh g^{-1}, increased to 161 $mAhg^{-1}$ by the fifth cycle. The anomaly observed during the first few cycles disappeared quickly and very stable cycle performance were obtained as described above. This phenomenon is even more significant when starting at very high current densities. The blue data points in Fig. 7a show the rate capability for the same sample, but starting the charge at 2.2 C (374 mA g^{-1}). The initial discharge capacity was very low (30 mAh g^{-1}) but increased to 89 mAh g^{-1} by the tenth cycle, suggsting that a "formation" or conditioning period occurs. Furthermore, at any current rate essentially the same capacity is achieved on extended cycling, but that value is attained more efficiently by starting at low current rates and increasing the current density, rather than starting at a high current rate and decreasing it. The cell starting at the fast rate of 2.2 C (blue curve) reaches "optimum capacity" of 135 mAh g^{-1} after 160 cycles of cycling at slow rates, but the cell starting at 0.1 C (red curve) reaches that same optimum capacity at 2.2 C after only 35 cycles (indicated by black arrows). Thus, a period of time at a low rate is necessary in order to achieve optimum capacity at any current density. This characteristic is due to the rigid surface layer. Electrode conditioning has been observed for other materials as well, and is often attributed to the need for full electrolyte penetration into the electrode mass, amongst other factors. In this case, however, Fe_2P displays considerable hardness along with high electronic conductivity,[28,10] and this means that additional energy may be required for egress and ingress of lithium through the compact layer within the first few charge and discharge processes. We observed that less "conditioning" was necessary for sample B, for example, which contained less phosphide. The electronically conductive Fe_2P surface can only be successfully activated and fully utilized after the creation of the paths for lithium migration, which are hindered by the hard compact layer during the first few cycles. As a consequence, the notable increase in capacities for the first few cycles suggests that $LiFePO_4$ with an Fe_2P coating would greatly benefit from slow charging during the first several cycles or a trickle charge, although it was not applied in this work.

Conclusions

The preparation of $LiFePO_4$ from Fe(III) [or Fe(II)] precursors typically requires processing treatment under inert or reducing atmospheres. These conditions determine the composition and fraction of surface species present, which in turn controls the electrochemical performance. While XRD provides useful information on bulk composition, it cannot detect the nanocrystalline or amorphous constituents on the surface of the particles that actually give rise to the

enhanced electrochemistry. These can be quantitatively determined by a combination of Mössbauer and XPS. The results show that under all but the most mild conditions, both FeP and Fe_2P, along with the by-product Li_3PO_4, are formed on the surface via surface reduction at temperatures as low as 600°C. A small amount of metallic Fe_2P gives rise to greatly enhanced electrochemical performance, with an optimum content between 5–10 wt %. The Fe_2P contribution increases with the severity of the reducing conditions, whereas the fraction of FeP remains essentially constant and has a more minor effect on the electrochemical properties. This is irrespective of the carbon content. The carbon and Li_3PO_4 are situated on the outer surface of the crystallites, whereas Fe_2P is located on the inner surface (next to $LiFePO_4$). This surface profile explains the significant capacity increase observed during initial cycling, as the electrodes are "conditioned" by microcracking of the surface films that allows access to the active material. For optimal electrochemical behavior, the Fe_2P surface layer should be as thin as possible.

Acknowledgments

This research was supported by funding from NSERC (Canada) and FQRNT (Quebec). L.F. Nazar gratefully thanks the NSERC for funding through the Canada Research Chair program.

University of Waterloo assisted in meeting the publication costs of this article.

References

1. A. K. Padhi, K. S. Nanjundaswamy, and J. B. Goodenough, *J. Electrochem. Soc.*, **144**, 1188 (1997).
2. N. Ravet, Y. Chouinard, J. F. Magnan, S. Besner, M. Gauthier, and M. Armand, *J. Power Sources*, **97–98**, 503 (2001); N. Ravet, J. B. Goodenough, S. Besner, M. Simoneau, P. Hovington, and M. Armand, Abstract 127, The Electrochemical Society and The Electrochemical Society of Japan Meeting Abstracts, Vol. 99-2, Honolulu, HI, Oct 17–22, 1999.
3. H. Huang, S. C. Yin, and L. F. Nazar, *Electrochem. Solid-State Lett.*, **4**, A170 (2001).
4. Z. Chen and J. R. Dahn, *J. Electrochem. Soc.*, **149**, A1184 (2002).
5. P. S. Herle, B. Ellis, N. Coombs, and L. F. Nazar, *Nat. Mater.*, **3**, 147 (2004).
6. J. Wolfenstine and J. Allen, *J. Power Sources*, **142**, 389 (2005).
7. D. Morgan, A. Van der Ven, and G. Ceder, *Electrochem. Solid-State Lett.*, **7**, A30 (2004).
8. M. S. Whittingham, Y. Song, S. Lutta, P. Y. Zavalij, and N. A. Chernova, *J. Mater. Chem.*, **15**, 3362 (2005).
9. K. F. Hsu, S. Y. Tsay, and B. J. Hwang, *J. Mater. Chem.*, **14**, 2690 (2004); M. Gaberscek, R. Dominko, M. Bele, M. Remskar, D. Hanzel, and J. Jamnik, *Solid State Ionics*, **176**, 1801 (2005).
10. H. Fujii, T. Hokabe, T. Kamigaichi, and T. Okamoto, *J. Phys. Soc. Jpn.*, **43**, 41 (1977).
11. A. C. Larson and R. B. Von Dreele, GSAS, Technical Report NM87545, Los Alamos National Laboratory, Los Alamos, NM (1994); B. H. Toby, *J. Appl. Crystallogr.*, **34**, 210 (2001).
12. S. H. Li, J. R. De Wijn, P. Layrolle, and K. de Groot, *J. Biomed. Mater. Res.*, **61**, 109 (2002); C. H. Lee, K. J. Lee, H. G. Jeong, and S. W. Kim, *Adv. Polym. Technol.*, **19**, 97 (2000); V. Padareva, S. DJoumalisky, N. Touleshkov, and G. Kirov, *J. Mater. Sci. Lett.*, **17**, 107 (1998).
13. G. Lewis and C. E. Myers, *J. Phys. Chem.*, **67**, 1289 (1963).
14. B. Ellis, P. Subramanya Herle, Y.-H. Rho, and L. F. Nazar, *Faraday Discuss.*, **134**, 119 (2007).
15. S.-Y. Chung and Y.-M. Chiang, *Electrochem. Solid-State Lett.*, **6**, A278 (2003).
16. A. Yamada, S. C. Chung, and K. Hinokuma, *J. Electrochem. Soc.*, **148**, A224 (2001); A. S. Andersson, J. O. Thomas, B. Kalska, and L. Häggström, *Electrochem. Solid-State Lett.*, **3**, 66 (2000); A. A. M. Prince, S. Mylswamy, T. S. Chan, R. S. Liu, B. Hannoyer, M. Jean, C. H. Shen, S. M. Huang, J. F. Lee, and G. X. Wang, *Solid State Commun.*, **132**, 455 (2004).
17. R. L. McCally, J. S. Morgan, T. J. Kistenmacher, and K. Moorjani, *J. Appl. Phys.*, **63**, 4124 (1988); R. Wäppling, L. Häggström, S. Rundqvist, and E. Karlsson, *J. Solid State Chem.*, **3**, 276 (1971); R. E. Bailey and J. F. Duncan, *Inorg. Chem.*, **6**, 1444 (1967); L. Häggström and A. Narayanasamy, *J. Magn. Magn. Mater.*, **30**, 249 (1982).
18. M. Herstedt, M. Stjerndahl, A. Nyten, T. Gustafsson, H. Rensmo, H. Siegbahn, N. Ravet, M. Armand, J. O. Thomas, and K. Edström, *Electrochem. Solid-State Lett.*, **6**, A202 (2003).
19. C. D. Wagner, A. V. Naumkin, A. Kraut-Vass, J. W. Allison, C. J. Powell, and J. R. Rumble, Jr., NIST X-ray Photoelectron Spectroscopy Database, http://srdata.nist.gov/xps/, 2003.
20. D. Aurbach, I. Weissman, and A. Schechter, *Langmuir*, **12**, 3991 (1996); S. Shiraishi, K. Kanamura, and Z. Takehara, *Langmuir*, **13**, 3542 (1997); T. A. Carlson, in *Photoelectron and Auger Spectroscopy*, Plenum, New York (1975), Appendix 3; D. Briggs and M. P. Seah, in *Practical Surface Analysis*, 2nd ed., Vol. 1, John Wiley & Sons, New York (1990).
21. V. V. Atuchin, V. G. Kesler, N. Y. Maklakova, L. D. Pokrovsky, and V. N. Semenenko, *Surf. Interface Anal.*, **34**, 320 (2002).
22. T. Barr, *J. Vac. Sci. Technol. A*, **9**, 1793 (1991).
23. This empirical prediction determines that in going from a simple oxide (A_2O) to a complex oxide such as a phosphate ($A_2P_3O_l$), that the A–O bond is generally made more ionic, whereas the P–O bond becomes more covalent. Because the XPS binding energy is a semiquantitative measure of the electron density around the atom being probed, this results in an increase in the lithium binding energy, and the opposite effect for phosphorus. In accordance, the P 2p peak in P_2O_5 at 135.3 eV shifts to lower binding energy (133.5 eV) in $LiFePO_4$.
24. N. S. McIntyre and D. G. Zetaruk, *Anal. Chem.*, **49**, 1521 (1977).
25. C. D. Wagner, L. E. Davis, M. V. Zeller, J. A. Taylor, R. Raymond, and L. H. Gale, *Surf. Interface Anal.*, **3**, 211 (1981); H. Berthou and C. K. Jørgensen, *Anal. Chem.*, **47**, 482 (1975).
26. V. V. Nemoskalenko, V. V. Didyk, V. P. Krivitskii, and A. I. Senkevich, *Russ. J. Inorg. Chem.*, **28**, 1239 (1983).
27. J. S. Pan, A. T. S. Wee, C. H. A. Huan, H. S. Tan, and K. L. Tan, *J. Appl. Phys.*, **80**, 6655 (1996); V. V. Atuchin, V. G. Kesler, N. Yu. Maklakova, L. D. Pokrovsky, and V. N. Semenenko, *Surf. Interface Anal.*, **34**, 320 (2002).
28. J. Nowacki, *Surf. Coat. Technol.*, **151–152**, 114 (2002).
29. A. M. Andersson, D. P. Abraham, R. Haasch, S. MacLaren, J. Liu, and K. Amine, *J. Electrochem. Soc.*, **149**, A1358 (2002).
30. S. C. Yin, Y. H. Rho, I. Swainson, and L. F. Nazar, *Chem. Mater.*, **18**, 1901 (2006).